

1 **Modeling groundwater responses to climate change in the Prairie Pothole Region**

2

3

4

5

6 Zhe Zhang¹, Yanping Li^{1*}, Michael Barlage², Fei Chen², Gonzalo Miguez-Macho³, Andrew Ireson¹,

7

Zhenhua Li¹

8

9

¹Global Institute for Water Security, University of Saskatchewan, Saskatoon, SK, Canada

10

²National Center for Atmospheric Research, Boulder, Colorado, USA

11

³Nonlinear Physic Group, Faculty of Physics, Universidade de Santiago de Compostela, Galicia, Spain

12

13 Abstract

14 Shallow groundwater in the Prairie Pothole Region (PPR) is recharged predominantly by snowmelt
15 in the spring and supplies water for evapotranspiration through the summer and fall. This two-way
16 exchange is underrepresented in current land surface models. Furthermore, the impacts of climate
17 change on the groundwater recharge rates are uncertain. In this paper, we use a coupled land and
18 groundwater model to investigate the hydrological cycle of shallow groundwater in the PPR and
19 study its response to climate change at the end of the 21st century. The results show that the model
20 reasonably simulates the water table depth (WTD) and the timing of recharge processes, but
21 predicts deep WTD in mountainous region in Alberta. The most significant change under future
22 climate conditions occurs in the winter, when warmer temperature changes the rain/snow
23 partitioning, delaying the time for snow accumulation/soil freezing while bring forward early
24 melting/thawing. Such changes lead to an earlier start to a longer recharge season, but with lower
25 recharge rates. Different signals are shown in the eastern and western PPR in the future summer,
26 with reduced precipitation and drier soils in the east but little change in the west. The annual
27 recharge increased by 25% and 50% in the eastern and western PPR, respectively. Additionally,
28 we found the mean and seasonal variation of the simulated WTD are sensitive to soil properties
29 and fine-scale soil information is needed to improve groundwater simulation on regional scale.

30

31 Keywords: Groundwater, Recharge, Climate Change, Prairie Pothole Region, Hydrological Cycle,

32 Introduction

33 The Prairie Pothole Region (PPR) in North America is located in a semi-arid and cold region,
34 where evapotranspiration (ET) exceeds precipitation (PR) in summer and near-surface soil is
35 frozen in winter (Gray, 1970; Granger and Gray, 1989; Hayashi et al., 2003; Pomeroy et al., 2007;
36 Ireson et al., 2013; Dumanski et al., 2015). These climatic conditions have introduced unique
37 hydrological characters to the groundwater flow in the PPR (Ireson et al., 2013). During winters,
38 frozen soils reduce permeability and snow accumulates on the surface, prohibiting infiltration (Niu
39 and Yang 2006; Mohammed et al., 2018). At the same time, the water table slowly declines due to
40 a combination of upward transport to freezing front by the capillary effect and discharge to rivers
41 (Ireson et al., 2013). In early springs, snowmelt becomes the dominant component of the
42 hydrological cycle and the melt water runs over frozen soil, with little infiltration contributing to
43 recharge. As the soil thaws, the increased infiltration capacity allows snowmelt recharge to the
44 water table, the previously upward water movement by capillary effect to reverse and move
45 downwards, and the water table to rise to its maximum level. In summers and falls, when high ET
46 exceeds PR, capillary rise may draw water from the groundwater aquifers to supply ET demands,
47 declining water table. These processes characterize the two-way water exchange between sub-
48 surface soils and groundwater aquifers.

49

50 Previous studies have suggested that substantial changes to groundwater interactions with above
51 soils are likely to occur under climate change (Tremblay et al., 2011; Green et al., 2011; Ireson et
52 al., 2013, 2015). Existing modeling studies on the impacts of climate change on groundwater are
53 either at global or basin/location-specific scales (Meixner et al., 2016). Global-level groundwater
54 studies focus on potential future recharge trends (Doll and Fiedler, 2008; Doll, 2009), yet coarse

55 resolution analysis from global climate models (GCMs) provided insufficient specificity to inform
56 decision making. Basin-scale groundwater studies connect the climate with groundwater-flow
57 models to understand the climate impacts on specific systems (Maxwell and Kollet, 2008; Kurylyk
58 and MacQuarrie, 2013; Dumanski et al., 2015). However, a knowledge gap exists in predicting the
59 effect of climate change over large regions (major river basins, states or group of states)
60 (Christensen et al., 2004; Green et al., 2011; Niraula et al., 2017).

61

62 Therefore, the objectives of this paper is to investigate the hydrological changes in groundwater in
63 PPR under climate change and understand the drivers for different hydrological processes. Our
64 goals are: 1) to model the water table dynamics in the PPR using a coupled land-groundwater
65 model; 2) to capture changes in the groundwater regime under climate change; and 3) to identify
66 major climatic and land surface processes that contribute to these changes in the PPR.

67

68 However, modeling the groundwater flows in PPR using LSMs is challenging because the
69 important two-way water exchange between unsaturated soils and groundwater aquifers was
70 neglected in previous LSMs. Recently, this two-way exchange has been implemented in coupled
71 land surface – groundwater models (LSM-GW). For example, Maxwell and Miller (2005) used a
72 groundwater model (ParFlow) coupled with the Common Land Model (CLM). They found that
73 the coupled and uncoupled model is very similar in simulated sensible heat flux (SH), ET, and
74 shallow soil moisture (SM), but are different greatly in runoff and deep SM. This is perhaps
75 because only downwards flow from soil to groundwater is considered. Later on, Kollet and
76 Maxwell (2008) incorporated the ET effect on redistributing moisture upward from shallow water
77 table depth (WTD) and found the surface energy partition is highly sensitive to a WTD ranging

78 from 1 – 5 m. More recently, Niu et al. (2011) implemented a simple groundwater model (SIMGM,
79 Niu et al., 2007), into the community Noah LSM with multi-parameterization options (Noah-MP
80 LSM), by adding an unconfined aquifer at the bottom of soil layers.

81

82 On the other hand, the soil freeze-thaw processes in cold region winters further complicate this
83 two-way exchange. Previous field studies have found that frozen soil not only influences the timing
84 and amount of downward recharge to aquifers by reducing the soil permeability (Koren et al., 1999;
85 Niu et al., 2006; Kelln et al., 2007), but may also induces upward water transport from aquifers to
86 soil freezing fronts (Spaans and Baker, 1996; Remenda et al., 1996; Hansson et al., 2004). In the
87 modeling community, there is a rich history in the frozen soil parameterizations. Earlier LSMs
88 assumed no significant heat transfer and soil water redistribution for sub-freezing temperature, for
89 example, in simplified SiB and BATS (Xue et al., 1991; Dickinson et al., 1993; Niu and Zeng,
90 2012). Koren et al. (1999) suggested that the frozen soil is permeable due to macropores exist in
91 soil structural aggregates, such as cracks, dead root passages, and worm holes. The NoahV3
92 adopted this scheme as its default option. Niu and Yang (2006) suggested to separate a model grid
93 into frozen and unfrozen patches, and these two patches have a linear effect on the soil hydraulic
94 properties. This treatment was incorporated into CLM 3.0 and Noah-MP in 2007 and 2011,
95 respectively.

96

97 Additionally, the spatial heterogeneity of soil moisture and WTD requires high-resolution
98 meteorological input that direct outputs from GCMs are too coarse to provide. Furthermore, in
99 GCMs, great uncertainties of simulated precipitation stem from choice of convection
100 parameterization schemes (Sherwood et al., 2014; Prein et al., 2015). An important approach to

101 improve precipitation simulation is to conduct dynamical downscale using the convection-
102 permitting model (CPM) (Ban et al., 2014; Prein et al., 2015; Liu et al., 2017). The CPM uses a
103 high spatial resolution (usually under 5-km) to explicitly resolve convection without activating
104 convection parameterization schemes. CPMs can also improve the representation of fine-scale
105 topography and spatial variations of surface fields (Prein et al., 2013). These CPM added-values
106 provide an excellent opportunity to investigate water table dynamics in the PPR.

107

108 In this paper, we use a physical process-based LSM (Noah-MP) coupled with a groundwater
109 dynamics model (MMF model). The coupled Noah-MP-MMF model is driven by two sets of
110 meteorological forcing for 13 years under current and future climate scenarios. These two sets of
111 meteorological dataset are from a CPM dynamical downscale project using the Weather Research
112 & Forecast (WRF) model with 4-km grid spacing covering the Contiguous U.S. and Southern
113 Canada (WRF CONUS, Liu et al., 2017). The paper is structured as follow: Section 2 introduces
114 the groundwater observations for WTD evaluation in the PPR, the coupled Noah-MP-MMF model,
115 and the meteorological forcing from the WRF CONUS project. Section 3 evaluates the model
116 simulated WTD timeseries and shows the groundwater budget and hydrological changes due to
117 climate change. Section 4 and 5 offer a broad discussion and conclusion.

118 2. Data and Methods

119 2.1 Observational data

120 Groundwater observation data were obtained through several agencies: (1) the United States
121 Geological Survey (USGS) National Water Information System in the U.S.
122 (<https://waterdata.usgs.gov/nwis/gw>), (2) the Alberta Environment
123 ([http://aep.alberta.ca/water/programs-and-services/groundwater/groundwater-observation-well-
124 network/default.aspx](http://aep.alberta.ca/water/programs-and-services/groundwater/groundwater-observation-well-
124 network/default.aspx)), (3) the Saskatchewan Water Security Agency
125 (<https://www.wsask.ca/Water-Info/Ground-Water/Observation-Wells/>).

126

127 Initially, groundwater data from 160 wells were acquired, 72 in the U.S., 43 from Alberta, and 45
128 from Saskatchewan. We used the following criteria to select qualified stations for our study and
129 evaluate our model performance against these observations:

- 130 1) the location of the wells are close to the PPR region;
- 131 2) a sufficiently long record during the simulation period. We define the observation
132 availability as the available observation period within the 13-year simulation period and
133 select wells with observation availability greater than 80%;
- 134 3) unconfined aquifers with shallow groundwater levels (mean WTD > - 5 m);
- 135 4) minimal anthropogenic effects (such as pumping or irrigation).

136

137 These criteria reduced the observation data to the record of 32 well records, with six in Alberta,
138 13 in Saskatchewan and 14 from the U.S. **Table 1** summarizes the information for each selected
139 well, and **Fig. 1(a)** shows the location of the wells in our study area. It is noteworthy that most of
140 the groundwater sites have more permeable deposits (sand and gravel) as provincial and state

141 agencies don't monitor low permeability formation. More information about the selecting criteria
142 are provided in the supplemental materials.

143

144 **Fig. 1** (a) Topography of the Prairie Pothole Region (PPR) and station location of rain gauges (black dots) and
145 groundwater wells (red diamonds); (b) Topography of the WRF CONUS domain, with the black box indicating the
146 PPR domain.

147

148 **Table 1.** Summary of the locations and aquifer type and soil type of the 33 selected wells.

149

150

151 2.2 Groundwater and Frozen Soil Scheme in Noah-MP

152 In the present study, we used the community Noah-MP LSM (Niu et al. 2011; Yang et al. 2011),
153 coupled with a GW model – the MMF model (Fan et al. 2007; Miguez-Macho et al., 2007). This
154 coupled model has been applied in many regional hydrology studies in offline mode (Miguez-
155 Macho and Fan 2012; Martinez et al., 2016) and coupled with regional climate models (Anyah et
156 al., 2008; Barlage et al., 2015). We present here a brief introduction to the MMF groundwater
157 scheme and the frozen soil scheme in Noah-MP, further details can be found in previous studies
158 (Fan et al., 2007; Miguez-Macho et al., 2007; Niu and Yang, 2006).

159

160 Fig. 2 is a diagram of the structure of 4 soil layers (0.1, 0.3, 0.6 and 1.0 m) and the underlying
161 unconfined aquifer in Noah-MP-MMF. The MMF scheme defines explicitly an unconfined aquifer
162 below the 2-m soil and an auxiliary soil layer stretching to the WTD, which varies in space and
163 time [m]. The thickness of this auxiliary layer (z_{aux} [m]) is also variable, depending on the WTD:

164
$$z_{aux} = \begin{cases} 1, & WTD \geq -3 \\ -2 - WTD, & WTD < -3 \end{cases} \quad (1)$$

165

166 The vertical fluxes include gravity drainage and capillary flux, solved from the Richards' equation,

167
$$q = K_{\theta} * \left(\frac{\partial \psi}{\partial z} - 1 \right), \quad K_{\theta} = K_{sat} * \left(\frac{\theta}{\theta_{sat}} \right)^{2b+3}, \quad \psi = \psi_{sat} * \left(\frac{\theta_{sat}}{\theta} \right)^b \quad (2)$$

168 where q is water flux between two adjacent layers [m/s], K_{θ} is the hydraulic conductivity [m/s] at
169 certain soil moisture content θ [m³/m³], ψ is the soil capillary potential [m] and b is soil pore size
170 index. The subscript *sat* denote saturated state. Therefore, the recharge flux from/to the layer above
171 WTD, R , can be obtained according to WTD:

$$R = \begin{cases} K_k * \left(\frac{\psi_i - \psi_k}{z_{soil(i)} - z_{soil(k)}} - 1 \right), & WTD \geq -2 \\ K_{aux} * \left(\frac{\psi_4 - \psi_{aux}}{(-2) - (-3)} - 1 \right), & -2 > WTD \geq -3 \\ K_{sat} * \left(\frac{\psi_{aux} - \psi_{sat}}{(-2) - (WTD)} - 1 \right), & WTD < -3 \end{cases} \quad (3)$$

173 In the first case, WTD is in the resolved soil layers and z_{soil} is the depth of soil layer with the
 174 subscript k indicating the layer containing WTD while i the layer above. The calculated water table
 175 recharge is then passed to the MMF groundwater routine.

176

177 The change of groundwater storage in the unconfined aquifer considers three components:
 178 recharge flux, river flux, and lateral flows:

$$\Delta S_g = (R - Q_r + \sum Q_{lat}) \quad (4)$$

180 where S_g [mm] is groundwater storage, Q_r [mm] is the water flux of groundwater-river exchange,
 181 and $\sum Q_{lat}$ [mm] are groundwater lateral flows to/from all surrounding grid cells. The groundwater
 182 lateral flow ($\sum Q_{lat}$) is the total horizontal flows between each grid cell and its neighbouring grid
 183 cells, calculated from Darcy's law with the Dupuit–Forchheimer approximation (Fan and Miguez-
 184 Macho 2010), as:

$$Q_{lat} = wT \left(\frac{h - h_n}{l} \right) \quad (5)$$

186 where w is the width of cell interface [m], T is the transmissivity of groundwater flow [m²/s], h
 187 and h_n are the water table head [m] of local and neighboring cell, and l is the length [m] between
 188 cells. T depends on hydraulic conductivity K and WTD:

$$T = \begin{cases} \int_{-\infty}^h K dz & WTD \geq -2 \\ \int_{-\infty}^{(z_{surf}-2)} K dz + \sum K_i * dz_i & WTD < -2 \end{cases} \quad (7)$$

189 For $WTD < -2$, K is assumed to decay exponentially with depth, $K = K_4 \exp(-z/f)$, K_4 is the
 190 hydraulic conductivity in the 4-th soil layer and f is the e-folding length and depends on terrain
 191 slope. For $WTD \geq -2$, i represents the number of layers between the water table and the 2-m bottom
 192 and z_{surf} is the surface elevation.

193
 194
 195 The river flux (Q_r) is also represented by a Darcy's law-type equation, which is the gradient
 196 between the groundwater head, local riverbed depth and parameterized river conductance:

$$Q_r = RC \cdot (h - z_{river}) \quad (8)$$

197
 198 with z_{river} is the depth of river bed [m] and RC is dimensionless river conductance, which depends
 199 on the slope of the terrain and equilibrium water table ($eqzwt$, [m]). Eq. (7) is a simplification
 200 which uses z_{river} rather than the water level in the river and, for this study, we only consider one-
 201 way discharge from groundwater to rivers. Finally, the change of WTD is calculated as the total
 202 fluxes fill or drain the pore space between saturation and the equilibrium soil moisture state (θ_{eq}
 203 [m^3/m^3]) in the layer containing WTD:

$$\Delta WTD = \frac{\Delta S_g}{(\theta_{sat} - \theta_{eq})} \quad (9)$$

204
 205 If ΔS_g is greater than the pore space in the current layer, the soil moisture content of current layer
 206 is saturated and the WTD rises to the layer above, updating the soil moisture content in the layer
 207 above as well. Vice versa for negative ΔS_g as water table declines and soil moisture decreases.

208

209 **Fig. 2** Structure of the Noah-MP LSM coupled with MMF groundwater scheme, the top 2-m soil of 4 layers whose
 210 thicknesses are 0.1, 0.3, 0.6 and 1.0 m. An unconfined aquifer is added below the 2-m boundary, including an auxiliary
 211 layer and the saturated aquifer. Positive flux of R denotes downward transport. Two water table are shown, one within
 212 the 2-m soil and one below, indicating that the model is capable to deal with both shallow and deep water table.

213
 214 There are two options in Noah-MP LSM for frozen soil permeability; option 1, the default option in Noah-MP, is from
 215 Niu and Yang (2006) and option 2 is inherited the Koren et al. (1999) scheme from NoahV3. Option 1 assumes that a
 216 model grid cell consists of permeable and impermeable patches and these patches integrate a linear effect on soil
 217 hydraulic properties. Thus, the total soil moisture in the grid cell is used to compute hydraulic properties as:

$$\theta = \theta_{ice} + \theta_{liq}$$

$$K = (1 - F_{frz})K_u = (1 - F_{frz})K_{sat} \left(\frac{\theta}{\theta_{sat}}\right)^{2b+3}$$

$$\psi = \psi_u = \psi_{sat} \left(\frac{\theta}{\theta_{sat}}\right)^{-b}$$

221 the subscript frz and u denote the frozen and unfrozen patches in the grid point. The water flux within in a model grid
 222 cell is:

$$q = (1 - F_{frz})q_u + F_{frz}q_{frz}$$

224 And the impermeable frozen soil fraction is parameterized as:

$$F_{frz} = e^{-\alpha(1-\theta_{ice}/\theta_{sat})} - e^{-\alpha}$$

226 $\alpha = 3.0$ is an adjustable parameter.

227
 228 However, the option 2 uses only the liquid water volume to calculate hydraulic properties and assumes a non-linear
 229 effect of frozen soil on permeability. Generally, option 1 assumes that soil ice has a smaller effect on infiltration and
 230 simulates more permeable frozen soil than option 2 (Niu et al., 2011). For this reason, the option 1 allows the soil
 231 water to move and redistribute more easily within the frozen soil and we decide to use option 1 in our study.

232 2.3 Forcing Data

233 The output from the WRF CONUS dataset (Liu et al. 2017) are used as meteorological forcing to
234 drive the Noah-MP-MMF model. The WRF CONUS project consists of two simulations. The first
235 simulation is referred as the current climate scenario, or control run (CTRL), from Oct 2000 to Sep
236 2013, and forced with the 6-hourly 0.7° ERA-Interim reanalysis data. The second simulation is a
237 perturbation to reflect the future climate scenario, closely following the pseudo global warming
238 (PGW) approach in previous works (Rasmussen et al., 2014). The PGW simulation is forced with
239 6-hourly ERA-Interim reanalysis data plus a delta climate change signal derived from an ensemble
240 of CMIP5 models under the RCP8.5 emission scenario and reflects the climate change signal
241 between the end of 21st and 20th century.

242

243 **Fig. 3** shows the annual precipitation in the PPR from 4-km WRF CONUS from the current climate
244 and 32-km North America Regional Reanalysis (NARR, another reanalysis dataset commonly
245 used for land surface model forcing). Both datasets show similar annual precipitation pattern and
246 bias patterns compared to observations: underestimating of precipitation in the east and
247 overestimating in the west. However, the WRF CONUS shows significant improvement of
248 percentage bias in precipitation $((\text{Model-Observation})/\text{Observation})$ over the western PPR. For the
249 consistency of the same source of data for current and future climate, the WRF-CONUS is the best
250 available dataset for the coupled land-groundwater study in the PPR.

251

252 **Fig. 3** Evaluation of the annual precipitation from WRF CONUS (top) and NARR (bottom) against rain gauge
253 observation.

254

255 For the future climate study, the precipitation and temperature of the PGW climate forcing are
256 shown in **Fig. 4** and **Fig. 5**. The WRF CONUS projects more precipitation in the PPR, except in
257 the southeast of the domain in summer, where it shows a precipitation reduction of about 50 to 100
258 mm. On the other hand, the WRF CONUS projects strongest warming occurring in the northeast
259 PPR in winter (**Fig. 5**), about 6–8 °C. Another significant warming signal occurs in summer in the
260 southeast of domain, corresponding to the reduction of future precipitation, as seen in **Fig. 4**.

261

262 **Fig. 4** Seasonal accumulated precipitation from current climate scenario(CTRL), future climate scenario (PGW) and
263 projected change (PGW-CTRL) in the forcing data.

264

265 **Fig. 5** Seasonal averaged temperature from CTRL, PGW, and the projected change (PGW-CTRL).

266

267 2.4 Model Setup

268 The two Noah-MP-MMF simulations representing the current climate and future climate are
269 denoted as CTRL and PGW, respectively. The initial groundwater levels are from a global 1-km
270 equilibrium groundwater map (Fan et al., 2013) and the equilibrium soil moisture for each soil
271 layer is calculated at the first model timestep with climatology recharge, spinning up for 500 years.
272 Since the model domain is at a different resolution than the input data, the appropriate initial WTD
273 at 4-km may be different than the average at 1-km. To properly initialize the simulation, we spin
274 up the model using the forcing of current climate (CTRL) for the years from 2000 to 2001
275 repeatedly (in total 10 loops).

276

277 Due to different data sources, the default soil types along the boundary between the U.S. and
278 Canada are discontinuous. Thus, we use the global 1-km fine soil data (Shangguan et al., 2014,
279 <http://globalchange.bnu.edu.cn/research/soilw>) in our study region. The soil properties for the
280 aquifer use the same properties as the lowest soil layer from the Noah-MP 2-m soil layers.

281 3. Results

282 3.1 Comparison with groundwater observations

283 According to the locations of 33 groundwater wells in **Table 1**, the simulated WTD from the
284 closest model grid points are extracted. **Fig. 6** shows the modeled WTD bias from the CTRL run.
285 We also select the monthly WTD timeseries from 8 sites, the observation are in black dots and
286 CTRL in blue lines. See supplemental materials for the timeseries of 33 sites. The model produces
287 reasonable values of mean WTD, the mean bias are smaller than 1 m in most of sites, except in
288 Alberta, where the model predicts deep bias in mountainous region. The model also successfully
289 captures the annual cycle of WTD, which rises in spring and early summer, because of snowmelt
290 and rainfall recharge, and declines in summer and fall, because of high ET, and in winter because
291 of frozen near-surface soil. In all observations, the timing of water table rising and dropping is
292 well simulated, as the timing and amount of infiltration and recharge in spring is controlled by the
293 freeze-thaw processes in seasonally frozen soil.

294

295 **Fig. 6.** WTD (m) bias from CTRL simulation and timeseries from 8 groundwater wells in PPR. See Table 2 CTRL
296 column for the model statistics and supplemental materials for complete timeseries from 33 wells.

297

298 On the other hand, the model simulated WTD seasonal variation is smaller than observations. The
299 small seasonal variation could be due to the misrepresentation between the lithology from the
300 observational surveys and the soil types in the model grids. As mentioned in Section 2.2, the
301 groundwater aquifer uses the same soil types as the bottom layer of the resolved 2-m soil layers.
302 While sand and gravel are the dominant lithology in most of the sites, they are mostly clay and
303 loam in the model (Table 1). For sandy soil reported in most of the sites, small capacity and fast
304 responses to infiltration lead to large water table fluctuations, whereas, in the model, clay and loam
305 soil allows low permeability and large capacity, and smoothens responses to recharge and capillary

306 effects. Furthermore, the 4-layer soils are vertically homogeneous in soil type and the groundwater
307 model uses the lowest level soil type as the aquifer lithology. For many part of the PPR, where
308 groundwater level are perched at the top 5-m due to a layer called glacial till. This geohydrological
309 characteristics cannot be reflected in this model and contribute to the deep WTD bias simulated in
310 Alberta. This shortcoming of the model was also reported in a study taken place in the Amazon
311 rainforest (Miguez-Macho et al., 2012).

312

313 3.2 Climate change signal in Groundwater fluxes

314 The MMF groundwater model simulates three components in the groundwater water budget, the
315 recharge flux (R), lateral flow (Q_{lat}), and discharge flux to rivers (Q_r). Because the topography is
316 usually flat in the PPR, the magnitude of groundwater lateral transport is very small (Q_{lat} less than
317 5 mm per year). On the other hand, the shallow water table in the PPR region is higher than the
318 local river bed, thus, the Q_r term is always discharging from groundwater aquifers to rivers. As a
319 result, the recharge term is the major contributor to the groundwater storage in the PPR, and its
320 variation (usually between -100 to 100 mm) dominates the timing and amplitude of the water table
321 dynamics. The seasonal accumulated total groundwater fluxes in the PPR ($R+Q_{lat} - Q_r$) are
322 shown in **Fig. 7**. The positive (negative) flux in blue (red) means the groundwater aquifer is gaining
323 (losing) water, causing the water table to rises (decline).

324

325 **Fig. 7** Seasonal accumulated total groundwater fluxes ($R+$) for current climate (CTRL, top), future climate (PGW,
326 middle) and projected change (PGW-CTRL, bottom) in forcing data. Black dashed lines in PGW-CTRL separate the
327 PPR into eastern and western halves.
328

329 Under current climate conditions, the total groundwater flux show strong seasonal fluctuations,
330 consistent with the WTD timeseries shown in **Fig. 6**. On average, in fall (SON) and winter (DJF),
331 there is a 20-mm negative recharge, driven by the capillary effects and drawing water from aquifer
332 to dry soil above. Spring (MAM) is usually the season with a strong positive recharge because
333 snowmelt provides a significant amount of water, and soils thawing allow infiltration. The large
334 amount of snowmelt water contributes to more than 100 mm of positive recharge in the eastern
335 domain. It is until summer (JJA), when strong ET depletes soil moisture and results in about 50
336 mm of negative recharge.

337

338 Under future climate conditions, the increased PR in fall and winter leads to wetter upper soil
339 layers, resulting in a net positive recharge flux (PGW – CTRL in SON and DJF). However, the
340 PGW summer is impacted by increased ET under a warmer and drier climate, due to higher
341 temperature and less PR. As a result, the groundwater uptake by the capillary effect is more critical
342 in the future summer. Furthermore, there is a strong east-to-west difference in the total
343 groundwater flux change from PGW to CTRL. In the eastern PPR, the change in total groundwater
344 flux exhibits obvious seasonality while the model projects persistent positive groundwater fluxes
345 in the western PPR.
346

347 3.3 Water budget analysis

348 **Fig. 8** and **Fig. 9** show the water budget analysis for the eastern and western PPR (divided by the
349 dotted line in 103° W in Fig. 7), respectively. Four components are presented in the figures, i.e.
350 (1) PR and ET; (2) surface and underground runoff (*SFCRUN* and *UDGRUN*); and surface
351 snowpack; (3) the change of soil moisture storage and (4) groundwater fluxes and the change of
352 storage. In current and future climate, these budget terms are plotted in annual accumulation ((a)
353 and (b) for CTRL and PGW), whereas their difference are plotted in each month individually ((c)
354 for PGW-CTRL).

355

356 Under current climate conditions, during snowmelt infiltration and rainfall event, water infiltrates
357 into the top soil layer, travels through the soil column and exits the bottom of the 2-m boundary,
358 hence, the water table rises. During the summer dry season, ET is higher than PR and the soil
359 layers lose water through ET, therefore, the capillary effect takes water from the underlying aquifer
360 and the water table declines. In winter, the near-surface soil in the PPR is seasonally frozen, thus,
361 a redistribution of subsurface water to the freezing front results in negative recharge, and the water
362 table declines.

363

364 In the eastern PPR, the effective precipitation (PR-ET) is found to increase from fall to spring, but
365 decrease in summer in PGW (**Fig. 8(1c)**). Warmer falls and winters in PGW, together with
366 increased PR, not only delay snow accumulation and bring forward snowmelt, but also change
367 the precipitation partition – more as rain and less as snow. This warming causes up to 20 mm of
368 snowpack loss (**Fig.8(2c)**). The underground runoff starts much earlier in PGW (December)
369 (**Fig.8(2b)**) than in CTRL (February) (**Fig.8(2a)**). On the other hand, the warming in PGW also

370 changes the partitioning of soil ice and soil water in subsurface soil layers (**Fig. 8(3c)**). For late
371 spring in PGW, the springtime recharge in the future is significantly reduced due to early melting
372 and less snowpack remaining (**Fig. 8(4c)**). In the PGW summer, reduced PR (50 mm less) and
373 higher temperatures (8 °C warmer) lead to reduction in total soil moisture, and a stronger negative
374 recharge from the aquifer. Therefore, the increase of recharge from fall to early spring compensates
375 the recharge reduction due to stronger ET in summer in the eastern PPR, and changes little in the
376 annual mean groundwater storage (1.763 mm per year).

377

378 **Fig. 8** Water budget analysis in the eastern PPR in (a) CTRL, (b) PGW and (c) PGW – CTRL. Water budget terms
379 include: (1) *PR & ET*, (2) surface snow, surface runoff and underground runoff (*SNOW*, *SFCRUN*, and *UDGRUN*),
380 (3) change of soil moisture storage (soil water, soil ice and total soil moisture, ΔSMC) and (4) groundwater fluxes
381 and the change of groundwater storage (R , Q_{lat} , Q_r , ΔS_g). The annual mean soil moisture change (PGW-CTRL) is
382 shown with black dashed line in (3). The Residual term is defined as $Res = (R+Q_{lat}-Q_r)-\Delta S_g$ in (4). Note that in (a)
383 and (b) the accumulated fluxes and change in storage are shown in lines, whereas in (c) the difference in (PGW-CTRL)
384 is shown for each individual month in bars.

385

386 These changes in water budget components in the western PPR (**Fig. 9**) are similar to those in the
387 eastern PPR (**Fig. 8**), except in summer. The reduction in summer PR in the western the PPR (less
388 than 5 mm reduction) is not as obvious as that in the eastern PPR (50 mm reduction) (**Fig. 4**). Thus,
389 annual mean total soil moisture in future is about the same as in current climate (Fig. 9(3c)) and
390 results in little negative recharge in PGW summer (**Fig. 9(4c)**). Therefore, the increase in annual
391 recharge is more significant (10 mm per year), an increase of about 50% of the annual recharge in
392 the current climate (20 mm per year) (**Fig. 9(4c)**).

393

394 **Fig. 9** Same as **Fig. 8**, but for the western PPR.

395

396 In both the eastern and western PPR, the water budget components for the groundwater aquifer are
397 plotted in **Fig. 8(4)** and **Fig. 9 (4)**, with the changes of each flux (PGW-CTRL) printed at the
398 bottom. The groundwater lateral flow is a small term in areal average and has little impact on the
399 groundwater storage. Nearly half of the increased recharge in both the eastern and western PPR is
400 discharged to river flux ($Q_r = 2.26$ mm out of $R = 4.15$ mm in the eastern PPR and $Q_r = 5.20$ mm
401 out of $R = 10.72$ mm in western PPR). Therefore, the groundwater storage change in the eastern
402 PPR (1.76 mm per year) is not as great as that in the western PPR (5.39 mm per year).

403

404 These two regions of the PPR show differences in hydrological response to future climate because
405 of the spatial variation of the summer PR. As shown in both **Fig. 4** (PGW-CTRL), **Fig. 8(1)** and
406 **Fig. 9(1)**, the reduction of future PR in summer in the eastern PPR is significant (50 mm). The
407 spatial difference of precipitation changes in the PPR further results in the recharge increase
408 doubling in the western PPR compared to the eastern PPR.

409

410 4. Discussion

411 4.1 Improving WTD Simulation

412 In Section 3.1, we show that model is capable of simulating the mean WTD in most sites, yet
413 predicts deep groundwater in Alberta and underestimates its seasonal variation. These results may
414 be due to misrepresentations between model default soil type and the soil properties in the
415 observational wells. To test this theory, an additional simulation, REP, is conducted by replacing
416 the default soil types in the locations of these 33 groundwater wells with sand-type soil, which is
417 the dominant soil types reported from observational surveys. The timeseries of the REP and default
418 CTRL are shown in Fig. 10 (also see supplemental materials for the complete 33 sites) and a
419 summary of the mean and standard deviation of the two simulations are provided in Table 2.

420

421 **Fig. 10** Same as Fig. 6, the timeseries of simulated WTD from both default model (blue) and replacing soil type
422 simulation, REP (red). REP is the additional simulation by replacing the default soil type in the model with sandy
423 soil type.

424

425 The REP simulation with sandy soil show two sensitive signals: (1) REP WTD are shallower than
426 the default simulation; (2) and exhibit stronger seasonal variation. These two signals can be
427 explained by the WTD equation in the MMF scheme:

$$428 \quad \Delta WTD = \frac{\Delta(R + Q_{lat} - Q_r)}{(\theta_{sat} - \theta_{eq})} \quad (10)$$

429 Eq. (10) represents that the change of WTD in a period of time is calculated by the total
430 groundwater fluxes, $\Delta(R + Q_{lat} - Q_r)$, divided by the available soil moisture capacity of current
431 layer $(\theta_{sat} - \theta_{eq})$. In REP simulation, the parameters θ_{sat} for the dominant soil type in
432 observational sites (sand/gravel) is smaller than those in default model grids (clay loam, sandy
433 loam, loam, loamy sand, etc.). Therefore, changing the θ_{sat} is essentially reducing the storage in

434 the aquifer and soil in this model grid. Given the same amount of groundwater flux, in the REP
435 simulation, the mean WTD is higher and the seasonal variation is stronger than the default CTRL
436 run.

437

438 In the REP simulation, we replaced soil type only at a limited number of sites because the
439 geological survey data in high resolution and large area extent is not yet available for the whole
440 PPR. At point scale, the WTD responses to climate change over these limited number of sites show
441 diverse results and uncertainties (see supplemental materials). For the rest of the domain, the
442 default soil type from global 1-km soil map is used. The REP modifications of soil types at point-
443 scale have small contribution to the water balance analysis (Fig. 8 & 9) at regional-scale. Our
444 results and conclusions for groundwater response to PGW doesn't change. We are currently
445 undertaking a soil property survey project in the PPR region to obtain soil properties at high spatial
446 resolution, both horizontal and vertical. This may provide better opportunity to improve WTD
447 simulation as well as assess climate-groundwater interaction in future studies.

448

449 4.2 Climate change Impacts on Groundwater Hydrological Regime

450 Climate change induced warming in high-latitudes winter and increased precipitation, including a
451 higher liquid fraction, in PGW winter results in later snow accumulation, higher winter recharge
452 and earlier melting in spring. Such changes in snowpack loss have been hypothesized in
453 mountainous as well as high-latitude regions (Taylor et al 2013; Ireson et al., 2015; Meixner et al.,
454 2016; Musselman et al., 2017).

455

456 In addition to the amount of recharge, the shift of recharge season is also noteworthy. Under current
457 climate conditions in spring, soil thawing (in March) is generally later than snowmelt (in February)
458 by a month in the PPR. Thus, the snowmelt water in pre-thaw spring would either re-freeze after
459 infiltrating into partially frozen soil or become surface runoff. Under the PGW climate, the warmer
460 winter and spring allows snowmelt and soil thaw to occur earlier in the middle of winter (in January
461 and February, respectively). As a result, the recharge season starts earlier in December, and last
462 longer until June, results in longer recharge season but with lower recharge rate.

463
464 Future projected increasing evapotranspiration demand in summer desiccates soil moisture,
465 resulting in more water uptake from aquifers to subsidize dry soil in the future summer. This
466 groundwater transport to soil moisture is similar to the “buffer effect” documented in an offline
467 study in the Amazon rainforest (Pokhrel et al., 2014). In , shallow water tables exist in the critical
468 zone, where WTD ranges from 1 to 5 meters below surface and could exert strong influence on
469 land energy and moisture fluxes feedback to the atmosphere (Kollet and Maxwell, 2008; Fan ,
470 2015). Previous coupled atmosphere-land-groundwater studies at 30-km resolution showed that
471 groundwater could support soil moisture during summer dry period, but has little impacts on
472 precipitation in Central U.S. (Barlage et al., 2015). It would be an interesting topic to study the
473 integrated impacts of shallow groundwater to regional climate in the convection permitting
474 resolution (resolution < 5-km).

475
476 4.3 Fine-scale interaction between groundwater and Prairie pothole wetlands
477 Furthermore, groundwater exchange with prairie pothole wetlands are complicated and critical in
478 the PPR. Numerous wetlands known as potholes or sloughs provide important ecosystem services,

479 such as providing wildlife habitats and groundwater recharge (Johnson et al., 2010). Shallow
480 groundwater aquifers may receive water from or lose water to prairie wetlands depending on the
481 hydrological setting. Depression-focused recharge generated by runoff from upland to depression
482 contributes to sufficient amount of water input to shallow groundwater (5-40 mm/year) (Hayashi
483 et al., 2016).

484

485 On the other hand, groundwater lateral flow exchange center of a wetland pond to its moist margin
486 is also an important components in the wetland water balance (van der Kamp and Hayashi, 2009;
487 Brannen, et al., 2015; Hayashi et al., 2016). However, this groundwater-wetland exchange
488 typically occurs on local scale (from 10 to 100 m) and thus, is challenging to in current land surface
489 models or climate models (resolution from 1 km to 100 km). In this paper, we focus on the
490 groundwater dynamics on regional scale, therefore, still unable to capture these small wetland
491 features in our model. We admit this challenge and are currently developing a sub-grid scheme to
492 represent open water wetlands as a fraction in a grid cell and calculate its feedback to regional
493 environments. Future studies on this topic will provide valuable insights on these key ecosystems
494 and their interaction under climate change.

495

496 Conclusion

497 In this study, a coupled land-groundwater model is applied to simulate the interaction between the
498 groundwater aquifer and soil moisture in the PPR. The climate forcing is from a dynamical
499 downscaling project (WRF CONUS), which uses the convection-permitting model (CPM)
500 configuration in high resolution. The goal of this study is to investigate the groundwater responses
501 to climate change, and to identify the major processes that contribute to these responses in the PPR.
502 To our knowledge, this is the first study applying CPM forcing in a hydrology study in this region.
503 We have three main findings:

504

505 (1) the coupled land-groundwater model shows reliable simulation of mean WTD, however
506 underestimates the seasonal variation of the water table against well observations. This could be
507 attributed to several reasons, including misrepresentation of topography and soil types, as well as
508 vertical homogenous soil layers used in the model. We further conducted an additional simulation
509 (REP) by replacing the model default soil types with sand-type soil and the simulated WTDs were
510 improved in both mean and seasonal variation. However, inadequacy of soil properties in deeper
511 layer and higher spatial resolution is still a limitation.

512

513 (2) Recharge markedly increases due to projected increased PR, particularly from fall to spring
514 under future climate conditions. Strong east-west spatial variation exists in the annual recharge
515 increases, 25% in the eastern and 50% in the western PPR. This is due to the significant projected
516 PR reduction in PGW summer in the eastern PPR but little change in the western PPR. This PR
517 reduction leads to stronger ET demand, which draws more groundwater uptake due to the capillary
518 effect, results in negative recharge in the summer. Therefore, the increased recharge from fall to

519 spring is consumed by ET in summer, and results in little change in groundwater in the eastern
520 PPR, while gaining water in the western PPR.

521

522 (3) The timing of infiltration and recharge are critically impacted by the changes in freeze-thaw
523 processes. Increased precipitation, combined with higher winter temperatures, results in later snow
524 accumulation/soil freezing, partitioned more as rain than snow, and earlier snowmelt/soil thaw.
525 This leads to substantial loss of snowpack, shorter frozen soil season, and higher permeability in
526 soil allowing infiltration. Late accumulation/freezing and early melting/thawing leads to an early
527 start of a longer recharge season from December to June, but with a lower recharge rate.

528

529 Our study has some limitations where future studies are encouraged:

530 (1) Despite the large number of groundwater wells in PPR, only a few are suitable for long-term
531 evaluation, due to data quality, anthropogenic pumping, and length of data record. As remote
532 sensing techniques advance, observing terrestrial water storage anomalies derived from the
533 GRACE satellite may provide substantial information on WTD, although the GRACE information
534 needs to be downscaled to a finer scale before comparisons can be made with regional hydrology
535 models at km-scale (Pokhrel et al., 2013).

536

537 (2) This study is an offline study of climate change impacts on groundwater. It is important to
538 investigate how shallow groundwater in the earth's critical zone could interact with surface water
539 and energy exchange to the atmosphere and affect regional climate. This investigation would be
540 important to the central North America region (one of the land atmosphere coupling "hot spots",
541 Koster et al., 2004).

542

543 **Acknowledgments**

544 The authors Zhe Zhang, Yanping Li, Zhenhua Li gratefully acknowledge the support from the
545 Changing Cold Regions Network (CCRN) funded by the Natural Science and Engineering
546 Research Council of Canada (NSERC), as well as the Global Water Future project and Global
547 Institute of Water Security at University of Saskatchewan. Yanping Li acknowledge the support
548 from NSERC Discovery Grant. Fei Chen, Michael Barlage appreciate the support from the Water
549 System Program at the National Center for Atmospheric Research (NCAR), USDA NIFA Grants
550 2015-67003-23508 and 2015-67003-23460, NSF INFEW/T2 Grant #1739705, and NOAA CFDA
551 Grant #NA18OAR4590381. NCAR is sponsored by the National Science Foundation. Any
552 opinions, findings, conclusions or recommendations expressed in this publication are those of the
553 authors and do not necessarily reflect the views of the National Science Foundation.

554

555 Reference

556 Anyah, R. O., Weaver, C. P., Miguez-macho, G., Fan, Y. and Robock, A.: Incorporating water
557 table dynamics in climate modeling : 3 . Simulated groundwater influence on coupled land-
558 atmosphere variability, , 113, 1–15, doi:10.1029/2007JD009087, 2008.

559 Ban, N., Schmidli, J. and Schär, C.: Evaluation of the new convective-resolving regional climate
560 modeling approach in decade-long simulations, *J. Geophys. Res. Atmos.*, 119, 7889–7907,
561 doi:10.1002/2014JD021478.Received, 2014.

562 Barlage, M., Tewari, M., Chen, F., Miguez-Macho, G., Yang, Z. L. and Niu, G. Y.: The effect of
563 groundwater interaction in North American regional climate simulations with WRF/Noah-MP,
564 *Clim. Change*, 129(3–4), 485–498, doi:10.1007/s10584-014-1308-8, 2015.

565 Brannen, R., Spence, C. and Ireson, A.: Influence of shallow groundwater-surface water
566 interactions on the hydrological connectivity and water budget of a wetland complex, *Hydrol.*
567 *Process.*, 29(18), 3862–3877, doi:10.1002/hyp.10563, 2015.

568 Christensen NS, Wood AW, Voisin N, et al (2004) The Effects of Climate Change on the
569 Hydrology and Water Resources of the Colorado River Basin. *Clim Change* 62:337–363. doi:
570 10.1023/B:CLIM.0000013684.13621.1f

571 Dickinson RE, Henderson-Sellers A, Kennedy PJ (1993) Biosphere-Atmosphere Transfer Scheme
572 (BATS) Version 1e as Coupled to the NCAR Community Climate Model. NCAR Technical
573 Note, NCAR/TN-387+STR.

574 Döll, P. and Fiedler, K.: Global-scale modeling of groundwater recharge, *Hydrol. Earth Syst. Sci.*,
575 12(3), 863–885, doi:10.5194/hess-12-863-2008, 2008.

576 Döll, P.: Vulnerability to the impact of climate change on renewable groundwater resources: A
577 global-scale assessment, *Environ. Res. Lett.*, 4(3), doi:10.1088/1748-9326/4/3/035006, 2009.

578 Dumanski, S., Pomeroy, J. W. and Westbrook, C. J.: Hydrological regime changes in a Canadian
579 Prairie basin, *Hydrol. Process.*, 29(18), 3893–3904, doi:10.1002/hyp.10567, 2015.

580 Environment Canada: Municipal Water Use, 2009 Statistics, 2011 Munic. Water Use Rep., 24,
581 doi:En11-2/2009E-PDF Information, 2011.

582 Fan Y, Miguez-Macho G, Weaver CP, et al (2007) Incorporating water table dynamics in climate
583 modeling: 1. Water table observations and equilibrium water table simulations. *J Geophys*
584 *Res Atmos* 112:1–17. doi: 10.1029/2006JD008111

585 Fan, Y., Li, H. and Miguez-Macho, G.: Global patterns of groundwater table depth, *Science* (80-.),
586 339(6122), 940–943, doi:10.1126/science.1229881, 2013.

587 Fan, Y.: Groundwater in the Earth’s critical zones: Relevance to large-scale patterns and processes,
588 *Water Resour. Res.*, 3052–3069, doi:10.1002/2015WR017037.Received, 2015.

589 Granger RJ, Gray DM: Evaporation from natural non-saturated surface. *J. Hydrol.*, 111, 21–29,
590 1989.

591 Gray DM: Handbook on the Principles of Hydrology: With Special Emphasis Directed to Canadian
592 Conditions in the Discussion, Applications, and Presentation of Data. Water Information
593 Center: Huntington, New York, 1970. ISBN:0-912394-07-2

594 Green, T. R., Taniguchi, M., Kooi, H., Gurdak, J. J., Allen, D. M., Hiscock, K. M., Treidel, H. and
595 Aureli, A.: Beneath the surface of global change: Impacts of climate change on groundwater,
596 *J. Hydrol.*, 405(3–4), 532–560, doi:10.1016/j.jhydrol.2011.05.002, 2011.

597 Hayashi, M., Van Der Kamp, G. and Schmidt, R.: Focused infiltration of snowmelt water in
598 partially frozen soil under small depressions, *J. Hydrol.*, 270(3–4), 214–229,
599 doi:10.1016/S0022-1694(02)00287-1, 2003.

600 Hayashi, M., van der Kamp, G. and Rosenberry, D. O.: Hydrology of Prairie Wetlands:
601 Understanding the Integrated Surface-Water and Groundwater Processes, *Wetlands*, 36, 237–
602 254, doi:10.1007/s13157-016-0797-9, 2016.

603 Ireson, A. M., van der Kamp, G., Ferguson, G., Nachshon, U. and Wheeler, H. S.: Hydrogeological
604 processes in seasonally frozen northern latitudes: understanding, gaps and challenges,
605 *Hydrogeol. J.*, 21(1), 53–66, doi:10.1007/s10040-012-0916-5, 2013.

606 Ireson, A. M., Barr, A. G., Johnstone, J. F., Mamet, S. D., van der Kamp, G., Whitfield, C. J.,
607 Michel, N. L., North, R. L., Westbrook, C. J., DeBeer, C., Chun, K. P., Nazemi, A. and Sagin,
608 J.: The changing water cycle: the Boreal Plains ecozone of Western Canada, *Wiley Interdiscip.*
609 *Rev. Water*, 2(5), 505–521, doi:10.1002/wat2.1098, 2015.

610 Johnson, W. C., Werner, B., Guntenspergen, G. R., Voldseth, R. A., Millett, B., Naugle, D. E.,
611 Tulbure, M., Carroll, R. W. H., Tracy, J. and Olawsky, C.: Prairie Wetland Complexes as
612 Landscape Functional Units in a Changing Climate, *Bioscience*, 60(2), 128–140,
613 doi:10.1525/bio.2010.60.2.7, 2010.

614 Kelln C, Barbour L, Qualizza C (2007) Preferential Flow in a Reclamation Cover : Hydrological
615 and Geochemical Response. 1277–1289

616 Koren, V., Schaake, J., Mitchell, K., Duan, Q.-Y., Chen, F., & Baker, J. M. (1999). A
617 parameterization of snowpack and frozen ground intended for NCEP weather and climate
618 models. *Journal of Geophysical Research: Atmospheres*, 104(D16), 19569–19585.
619 <https://doi.org/10.1029/1999JD900232>

620 Koster, R. D., Dirmeyer, P. A., Guo, Z., Bonan, G., Chan, E., Cox, P., Gordon, C. T., Kanae, S.,
621 Kowalczyk, E., Lawrence, D., Liu, P., Lu, C.-H., Malyshev, S., McAvaney, B., Mitchell,
622 K., Mocko, D., Oki, T., Oleson, K., Pitman, A., Sud, Y. C., Taylor, C. M., Versegny, D.,
623 Vasic, R., Xue, Y. and Yamada, T.: Regions of Strong Coupling Between Soil Moisture and
624 Precipitation, *Science* (80-.), 305(5687), 1138 LP-1140 [online] Available from:
625 <http://science.sciencemag.org/content/305/5687/1138.abstract>, 2004.

626 Kollet SJ, Maxwell RM (2008) Capturing the influence of groundwater dynamics on land surface
627 processes using an integrated, distributed watershed model. *Water Resour Res* 44:1–18. doi:
628 10.1029/2007WR006004

629 Kurylyk, B. L. and MacQuarrie, K. T. B.: The uncertainty associated with estimating future
630 groundwater recharge: A summary of recent research and an example from a small unconfined
631 aquifer in a northern humid-continental climate, *J. Hydrol.*, 492, 244–253,
632 doi:10.1016/j.jhydrol.2013.03.043, 2013.

633 Liu, C., Ikeda, K., Rasmussen, R., Barlage, M., Newman, A. J., Prein, A. F., Chen, F., Chen, L.,
634 Clark, M., Dai, A., Dudhia, J., Eidhammer, T., Gochis, D., Gutmann, E., Kurkute, S., Li, Y.,
635 Thompson, G. and Yates, D.: Continental-scale convection-permitting modeling of the current
636 and future climate of North America, *Clim. Dyn.*, 49(1–2), 71–95, doi:10.1007/s00382-016-
637 3327-9, 2017.

638 Martinez, J. A., Dominguez, F. and Miguez-Macho, G.: Effects of a Groundwater Scheme on the
639 Simulation of Soil Moisture and Evapotranspiration over Southern South America, *J.*
640 *Hydrometeorol.*, 17(11), 2941–2957, doi:10.1175/JHM-D-16-0051.1, 2016.

641 Maxwell RM, Miller NL (2005) Development of a Coupled Land Surface and Groundwater
642 Model. 233–247

643 Maxwell, R. M. and Kollet, S. J.: Interdependence of groundwater dynamics and land-energy
644 feedbacks under climate change, *Nat. Geosci.*, 1(10), 665–669, doi:10.1038/ngeo315, 2008.

645 Meixner, T., Manning, A. H., Stonestrom, D. A., Allen, D. M., Ajami, H., Blasch, K. W.,
646 Brookfield, A. E., Castro, C. L., Clark, J. F., Gochis, D. J., Flint, A. L., Neff, K. L., Niraula,
647 R., Rodell, M., Scanlon, B. R., Singha, K. and Walvoord, M. A.: Implications of projected
648 climate change for groundwater recharge in the western United States, *J. Hydrol.*, 534, 124–
649 138, doi:10.1016/j.jhydrol.2015.12.027, 2016.

650 Miguez-Macho, G., Fan, Y., Weaver, C. P., Walko, R. and Robock, A.: Incorporating water table
651 dynamics in climate modeling: 2. Formulation, validation, and soil moisture simulation, *J.*
652 Miguez-Macho, G. and Fan, Y.: The role of groundwater in the Amazon water cycle: 1. Influence
653 on seasonal streamflow, flooding and wetlands, *J. Geophys. Res. Atmos.*, 117(15), 1–30,
654 doi:10.1029/2012JD017539, 2012.

655 Moeck, C., Brunner, P. and Hunkeler, D.: The influence of model structure on groundwater
656 recharge rates in climate-change impact studies, *Hydrogeol. J.*, 24(5), 1171–1184,
657 doi:10.1007/s10040-016-1367-1, 2016.

658 Mohammed, A. A., Kurylyk, B. L., Cey, E. E. and Hayashi, M.: Snowmelt Infiltration and
659 Macropore Flow in Frozen Soils: Overview, Knowledge Gaps, and a Conceptual Framework,
660 *Vadose Zo. J.*, 17(1), doi:10.2136/vzj2018.04.0084, 2018.

661 Musselman, K. N., Clark, M. P., Liu, C., Ikeda, K. and Rasmussen, R.: Slower snowmelt in a
662 warmer world, *Nat. Clim. Chang.*, 7(February), 214–220, doi:10.1038/NCLIMATE3225,
663 2017.

664 National Research Council: Groundwater fluxes across inter- faces. The National Academy Press,
665 85 pp, 2003

666 Niraula R, Meixner T, Dominguez F, et al (2017) How Might Recharge Change Under Projected
667 Climate Change in the Western U.S.? *Geophys Res Lett* 44:10,407-10,418. doi:
668 10.1002/2017GL075421

669 Niu, G.-Y., & Yang, Z.-L. (2006). Effects of Frozen Soil on Snowmelt Runoff and Soil Water
670 Storage at a Continental Scale. *Journal of Hydrometeorology*, 7(5), 937–952.
671 <https://doi.org/10.1175/JHM538.1>

672 Niu G, Yang Z, Dickinson RE, Gulden LE (2007) Development of a simple groundwater model
673 for use in climate models and evaluation with Gravity Recovery and Climate Experiment
674 data. 112:1–14. doi: 10.1029/2006JD007522

675 Niu, G. Y., Yang, Z. L., Mitchell, K. E., Chen, F., Ek, M. B., Barlage, M., Kumar, A., Manning,
676 K., Niyogi, D., Rosero, E., Tewari, M. and Xia, Y.: The community Noah land surface model
677 with multiparameterization options (Noah-MP): 1. Model description and evaluation with
678 local-scale measurements, *J. Geophys. Res. Atmos.*, 116(12), 1–19,
679 doi:10.1029/2010JD015139, 2011.

680 Niu G-Y, Zeng X (2012) Earth System Model, Modeling the Land Component of. In: *Climate*
681 *Change Modeling Methodology*. Springer New York, New York, NY, pp 139–168

682 Pokhrel, Y. N., Fan, Y., Miguez-Macho, G., Yeh, P. J. F. and Han, S. C.: The role of groundwater
683 in the Amazon water cycle: 3. Influence on terrestrial water storage computations and
684 comparison with GRACE, *J. Geophys. Res. Atmos.*, 118(8), 3233–3244,
685 doi:10.1002/jgrd.50335, 2013.

686 Pokhrel, Y. N., Fan, Y. and Miguez-Macho, G.: Potential hydrologic changes in the Amazon by
687 the end of the 21st century and the groundwater buffer, *Environ. Res. Lett.*, 9(8),
688 doi:10.1088/1748-9326/9/8/084004, 2014.

689 Pomeroy, J. W.: The cold regions hydrological model: a platform for basing process representation
690 and model structure on physical evidence, *Hydrol. Process.*, 21, 2650–2667, doi:10.1002/hyp,
691 2007.

692 Prein, A. F., Gobiet, A., Suklitsch, M., Truhetz, H., Awan, N. K., Keuler, K. and Georgievski, G.:
693 Added value of convection permitting seasonal simulations, , 2655–2677,
694 doi:10.1007/s00382-013-1744-6, 2013.

695 Prein, A. F., Langhans, W., Fosser, G., Ferrone, A., Ban, N., Goergen, K., Keller, M., Tölle, M.,
696 Gutjahr, O., Feser, F., Brisson, E., Kollet, S., Schmidli, J., Van Lipzig, N. P. M. and Leung,
697 R.: A review on regional convection-permitting climate modeling: Demonstrations, prospects,
698 and challenges, *Rev. Geophys.*, 53(2), 323–361, doi:10.1002/2014RG000475, 2015.

699 Rasmussen, K. L., Prein, A. F., Rasmussen, R. M., Ikeda, K. and Liu, C.: Changes in the convective
700 population and thermodynamic environments in convection-permitting regional climate
701 simulations over the United States, *Clim. Dyn.*, (0123456789), 1–26, doi:10.1007/s00382-
702 017-4000-7, 2017.

703 Remenda VH, van der Kamp G, Cherry JA (1996) Use of vertical profiles of • 180 to constrain
704 estimates of hydraulic conductivity in a thick, unfractured aquitard. 32:2979–2987

705 Shangguan W, Dai Y, Duan Q, et al (2014) *Journal of Advances in Modeling Earth Systems*. J
706 *Adv Model Earth Syst* 6:249–263. doi: 10.1002/2013MS000293. Received

707 Sherwood, S. C., Bony, S. and Dufresne, J.: Spread in model climate sensitivity traced to
708 atmospheric convective mixing, , doi:10.1038/nature12829, 2014.

709 Siebert, S., Burke, J., Faures, J. M., Frenken, K., Hoogeveen, J., Döll, P. and Portmann, F. T.:
710 Groundwater use for irrigation - A global inventory, *Hydrol. Earth Syst. Sci.*, 14(10), 1863–
711 1880, doi:10.5194/hess-14-1863-2010, 2010.

712 Smerdon, B. D.: A synopsis of climate change effects on groundwater recharge, *J. Hydrol.*, 555,
713 125–128, doi:10.1016/j.jhydrol.2017.09.047, 2017.

714 Statistics Canada: Quarterly Estimates of the Population of Canada, the Provinces and the
715 Territories, 11-3, Catalogue 91-001, Ottawa, 1996

716 Taylor, R. G.: Ground water and climate change, , 3(November 2012),
717 doi:10.1038/NCLIMATE1744, 2013.

718 Tremblay, L., Larocque, M., Anctil, F. and Rivard, C.: Teleconnections and interannual variability
719 in Canadian groundwater levels, *J. Hydrol.*, 410(3–4), 178–188,
720 doi:10.1016/j.jhydrol.2011.09.013, 2011.

721 UNESCO: *Groundwater Resources of the World and Their Use*, edited by I. Zektser and L. Everett,
722 Paris., 2004.

723 Van Der Kamp G, Hayashi M (2009) Groundwater-wetland ecosystem interaction in the
724 semiarid glaciated plains of North America. *Hydrogeol J* 17:203–214. doi: 10.1007/s10040-
725 008-0367-1

726 Xue Y, Sellers PJ, Kinter JL, Shukla J (1991) A Simplified Biosphere Model for Global Climate
727 Studies. *J Clim* 4:345–364. doi: 10.1175/1520-0442(1991)004<0345:ASBMFG>2.0.CO;2

728 Yang, Z. L., Niu, G. Y., Mitchell, K. E., Chen, F., Ek, M. B., Barlage, M., Longuevergne, L.,
729 Manning, K., Niyogi, D., Tewari, M. and Xia, Y.: The community Noah land surface model
730 with multiparameterization options (Noah-MP): 2. Evaluation over global river basins, *J.*
731 *Geophys. Res. Atmos.*, 116(12), 1–16, doi:10.1029/2010JD015140, 2011.

732

733

734 Table and Figure

735

736 **Table 1.** Summary of the locations and aquifer type and soil type of the 33 selected wells.

Site Name/ Site No.	Lat	Lon	Elev	Aquifer type	Aquifer Lithology	Model Elevation	Model Soil type
Devon 0162	53.41	-113.76	700.0	Unconfined	Sand	697.366	Sandy loam
Hardisty 0143	52.67	-111.31	622.0	Unconfined	Gravel	633.079	Loam
Kirkpatrick Lake 0229	51.95	-111.44	744.5	Semi-confined	Sandstone	778.311	Sandy loam
Metiskow 0267	52.42	-110.60	677.5	Unconfined	Sand	679.516	Loamy sand
Wagner 0172	53.56	-113.82	670.0	Surficial	Sand	670.845	Silt loam
Narrow Lake 252	54.60	-113.63	640.0	Unconfined	Sand	701.0	Clay loam
Baildon 060	50.25	-105.50	590.184	Surficial	-	580.890	Sandy loam
Beauval	55.11	-107.74	434.3	Intertill	Sand	446.5	Sandy loam
Blucher	52.03	-106.20	521.061	Intertill	Sand/Gravel	523.217	Loam
Crater Lake	50.95	-102.46	524.158	Intertill	Sand/Gravel/Clay	522.767	Loam
Duck Lake	52.92	-106.23	502.920	Surficial	Sand	501.729	Loamy sand
Forget	49.70	-102.85	606.552	Surficial	Sand	605.915	Sandy loam
Garden Head	49.74	-108.52	899.160	Bedrock	Sand/Till	894.357	Clay loam
Nokomis	51.51	-105.06	516.267	Bedrock	Sand	511.767	Clay loam
Shaunavon	49.69	-108.50	896.040	Bedrock	Sand/Till	900.433	Clay loam
Simpson 13	51.45	-105.18	496.620	Surficial	Sand	493.313	Sandy loam
Simpson 14	51.457	-105.19	496.600	Surficial	Sand	493.313	Sandy loam
Yorkton 517	51.17	-102.50	513.643	Surficial	Sand/Gravel	511.181	Loam
Agrium 43	52.03	-107.01	500.229	Intertill	Sand	510.771	Loam
460120097591803	46.02	-97.98	401.177	Alluvial	Sand/Gravel	400.381	Sandy loam
461838097553402	46.31	-97.92	401.168	-	Sand/Gravel	404.719	Clay loam
462400097552502	46.39	-97.92	409.73	-	Sand/Gravel	407.405	Sandy loam
462633097163402	46.44	-97.27	325.52	Alluvial	Sand/Gravel	323.728	Sandy loam
463422097115602	46.57	-97.19	320.40	Alluvial	Sand/Gravel	314.167	Sandy loam
464540100222101	46.76	-100.37	524.91	-	Sand/Gravel	522.600	Clay loam
473841096153101	47.64	-96.25	351.77	Surficial	Sand/Gravel	344.180	Loamy sand
473945096202402	47.66	-96.34	327.78	Surficial	Sand/Gravel	328.129	Sandy loam
474135096203001	47.69	-96.34	325.97	Surficial	Sand/Gravel	327.764	Sandy loam
474436096140801	47.74	-96.23	341.90	Surficial	Sand/Gravel	336.210	Sandy loam
475224098443202	47.87	-98.74	451.33	-	Sand/Gravel	450.463	Sandy loam
481841097490301	48.31	-97.81	355.61	-	Sand/Gravel	359.568	Clay loam
482212099475801	48.37	-99.79	488.65	-	Sand/Gravel	488.022	Sandy loam
CRN Well WLN03	45.98	-95.20	410.7	Surficial	Sand/Gravel	411.4	Sandy loam

737

738 **Table 2.** Summary of mean and standard deviation (std) of WTD from 33 groundwater wells, from
739 observation records (OBS), default model (CTRL) and replacing with sand soil simulation (REP).
740 Bold texts indicate improvement in the REP than the CTRL run.
741

Site Name/Number	Province	OBS_mean	CTRL_mean	REP_mean	OBS_std	CTRL_std	REP_std
Devon 0162	AB	-2.46	-2.69	-2.38	0.43	0.45	0.09
Hardisty 0143		-2.44	-8.91	-6.88	0.41	0.64	0.36
Kirkpatrick Lake 0229		-4.22	-4.03	-3.45	0.43	0.98	0.22
Metiskow 0267		-2.54	-5.39	-4.43	0.34	0.78	0.55
Narrow Lake 252		-2.31	-4.81	-3.75	0.28	0.60	0.51
Wagner 0172		-2.14	-8.06	-2.70	0.48	0.37	0.21
Baildon 060	SK	-2.80	-3.29	-3.20	0.47	0.58	0.30
Beauval		-3.78	-4.85	-4.20	0.44	0.56	0.32
Blucher		-2.20	-4.24	-2.16	0.3	0.92	0.26
Crater Lake		-4.33	-3.97	-3.64	1.1	0.4	0.28
Duck Lake		-3.65	-3.69	-3.17	0.54	0.41	0.62
Forget		-2.28	-2.37	-2.23	0.33	0.17	0.19
Garden Head		-3.67	-4.85	-3.77	0.88	0.70	0.30
Nokomis		-1.04	-2.70	-2.17	0.23	0.55	0.17
Shaunavon		-1.62	-4.41	-2.58	0.42	0.69	0.20
Simpson 13		-4.82	-4.83	-3.02	0.31	0.91	0.17
Simpson 14		-2.03	-2.61	-1.82	0.34	0.18	0.27
Yorkton 517		-2.87	-3.97	-1.98	0.8	0.46	0.32
Agrium 43		-2.66	-3.75	-3.38	0.32	1.05	0.36
460120097591803	ND	-1.44	-2.33	-1.63	0.56	0.24	0.50
461838097553402		-1.17	-2.32	-1.68	0.27	0.24	0.43
462400097552502		-4.9	-5.61	-5.37	0.29	0.09	0.17
462633097163402		-1.18	-1.49	-1.02	0.46	0.29	0.54
463422097115602		-1.36	-2.28	-1.66	0.34	0.23	0.49
464540100222101		-2.02	-3.64	-2.78	0.52	0.43	0.32
473841096153101	G15	-0.77	-1.48	-1.37	0.24	0.18	0.51
473945096202402	E01S	-1.59	-1.58	-1.56	0.32	0.24	0.51
474135096203001	G01	-0.72	-1.48	-1.30	0.33	0.25	0.54
474436096140801	E03	-2.44	-2.29	-1.96	0.39	0.21	0.40
475224098443202		-4.52	-4.28	-5.31	0.75	0.52	0.34
481841097490301		-4.39	-4.24	-4.58	0.79	0.28	0.17
482212099475801		-2.13	-2.32	-2.26	0.24	0.20	0.17
CRN WLN 03		-2.04	-2.18	-1.88	0.24	0.18	0.43

742

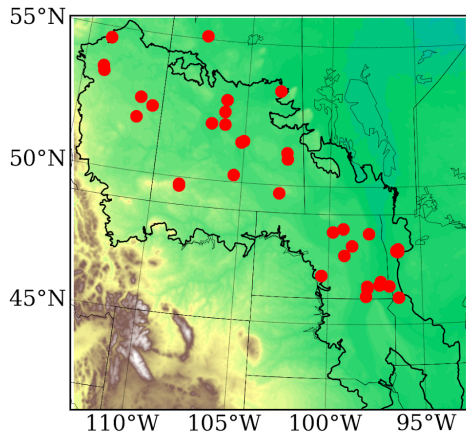
Site Name/Number	OBS_mean	CTRL_mean	REP_mean	OBS_std	CTRL_std	REP_std
Devon 0162	-2.46	-2.69	-2.38	0.43	0.45	0.09
Hardisty 0143	-2.44	-8.91	-6.88	0.41	0.64	0.36
Kirkpatrick Lake 0229	-4.22	-4.03	-3.45	0.43	0.98	0.22
Metiskow 0267	-2.54	-5.39	-4.43	0.34	0.78	0.55
Narrow Lake 252	-2.31	-4.81	-3.75	0.28	0.60	0.51
Wagner 0172	-2.14	-8.06	-2.70	0.48	0.37	0.21
Baildon 060	-2.80	-3.29	-3.20	0.47	0.58	0.30
Beauval	-3.78	-4.85	-4.20	0.44	0.56	0.32
Blucher	-2.20	-4.24	-2.16	0.3	0.92	0.26
Crater Lake	-4.33	-3.97	-3.64	1.1	0.4	0.28
Duck Lake	-3.65	-3.69	-3.17	0.54	0.41	0.62
Forget	-2.28	-2.37	-2.23	0.33	0.17	0.19

Garden Head	-3.67	-4.85	-3.77	0.88	0.70	0.30
Nokomis	-1.04	-2.70	-2.17	0.23	0.55	0.17
Shaunavon	-1.62	-4.41	-2.58	0.42	0.69	0.20
Simpson 13	-4.82	-4.83	-3.02	0.31	0.91	0.17
Simpson 14	-2.03	-2.61	-1.82	0.34	0.18	0.27
Yorkton 517	-2.87	-3.97	-1.98	0.8	0.46	0.32
Agrium 43	-2.66	-3.75	-3.38	0.32	1.05	0.36
460120097591803	-1.44	-2.33	-1.63	0.56	0.24	0.50
461838097553402	-1.17	-2.32	-1.68	0.27	0.24	0.43
462400097552502	-4.9	-5.61	-5.37	0.29	0.09	0.17
462633097163402	-1.18	-1.49	-1.02	0.46	0.29	0.54
463422097115602	-1.36	-2.28	-1.66	0.34	0.23	0.49
464540100222101	-2.02	-3.64	-2.78	0.52	0.43	0.32
473841096153101	-0.77	-1.48	-1.37	0.24	0.18	0.51
473945096202402	-1.59	-1.58	-1.56	0.32	0.24	0.51
474135096203001	-0.72	-1.48	-1.30	0.33	0.25	0.54
474436096140801	-2.44	-2.29	-1.96	0.39	0.21	0.40
475224098443202	-4.52	-4.28	-5.31	0.75	0.52	0.34
481841097490301	-4.39	-4.24	-4.58	0.79	0.28	0.17
482212099475801	-2.13	-2.32	-2.26	0.24	0.20	0.17
CRN WLN 03	-2.04	-2.18	-1.88	0.24	0.18	0.43

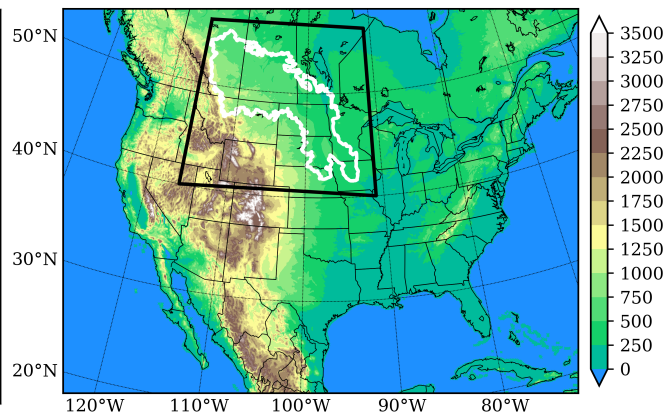
743
744

745
746

(a)



(b)

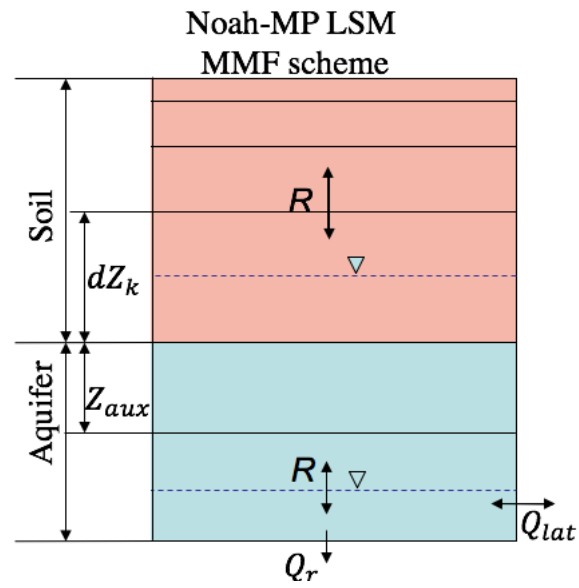


747
748

(b)
(c)

749 **Fig. 1** (a) Topography of the Prairie Pothole Region (PPR; black outline) and groundwater wells (red dots); (b) Topography
750 of the WRF CONUS domain, the black box indicates the PPR domain.
751

752

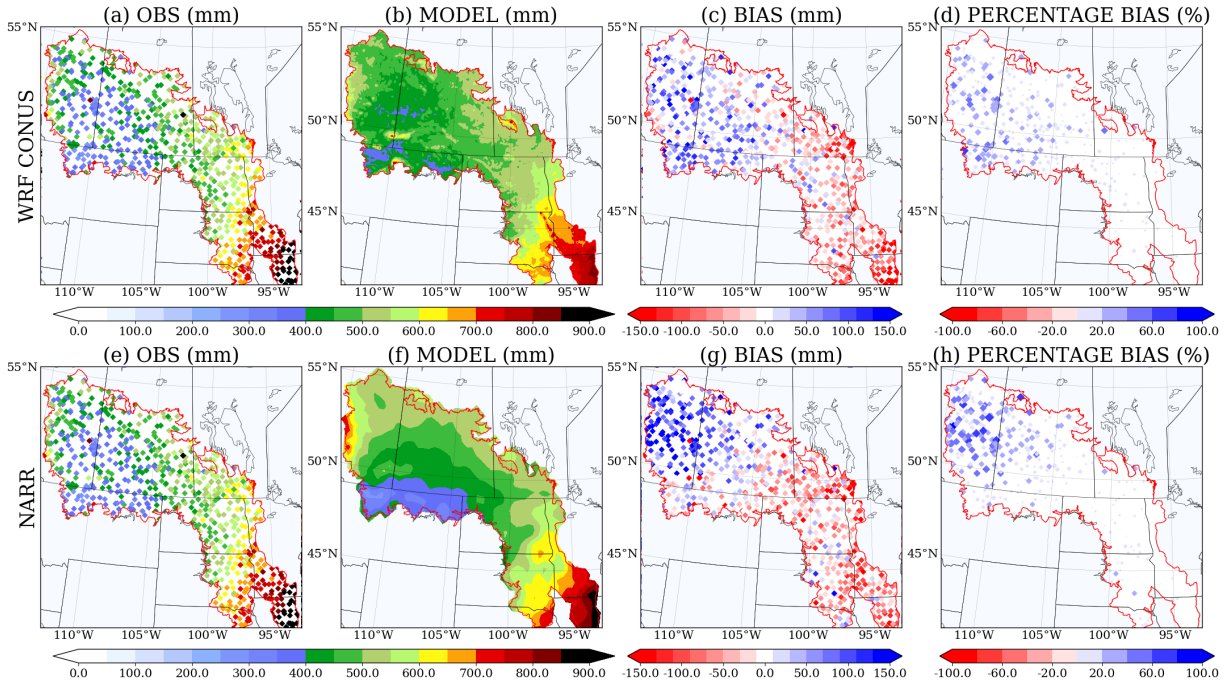


753

754 **Fig. 2** Structure of the Noah-MP LSM coupled with MMF groundwater scheme, the top 2-m soil of 4 layers whose thicknesses
755 are 0.1, 0.3, 0.6 and 1.0 m. An unconfined aquifer is added below the 2-m boundary, including an auxiliary layer and the saturated
756 aquifer. Positive flux of R denotes downward transport. Two water table are shown, one within the 2-m soil and one below,
757 indicating that the model is capable to deal with both shallow and deep water table.

758

759



760

761

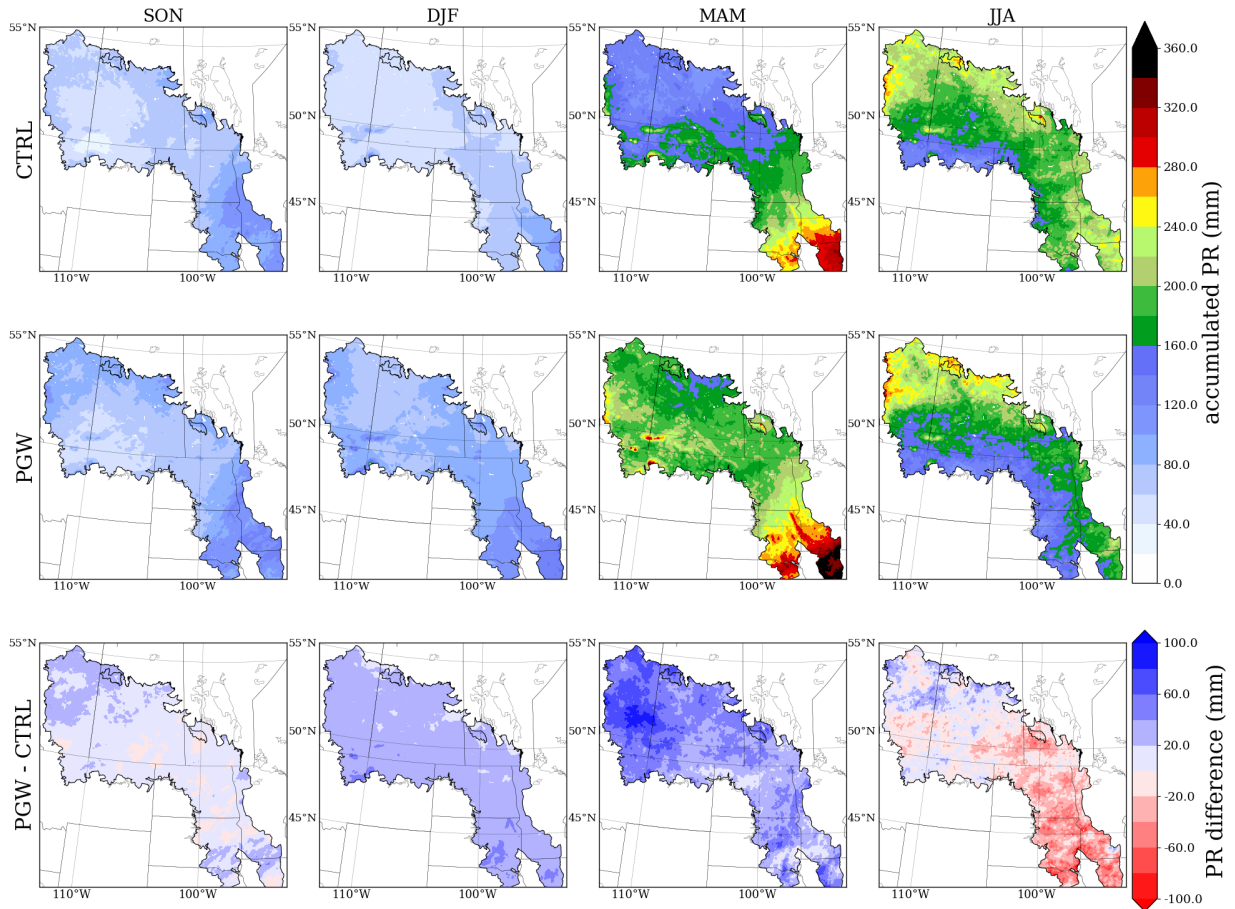
762

763

764

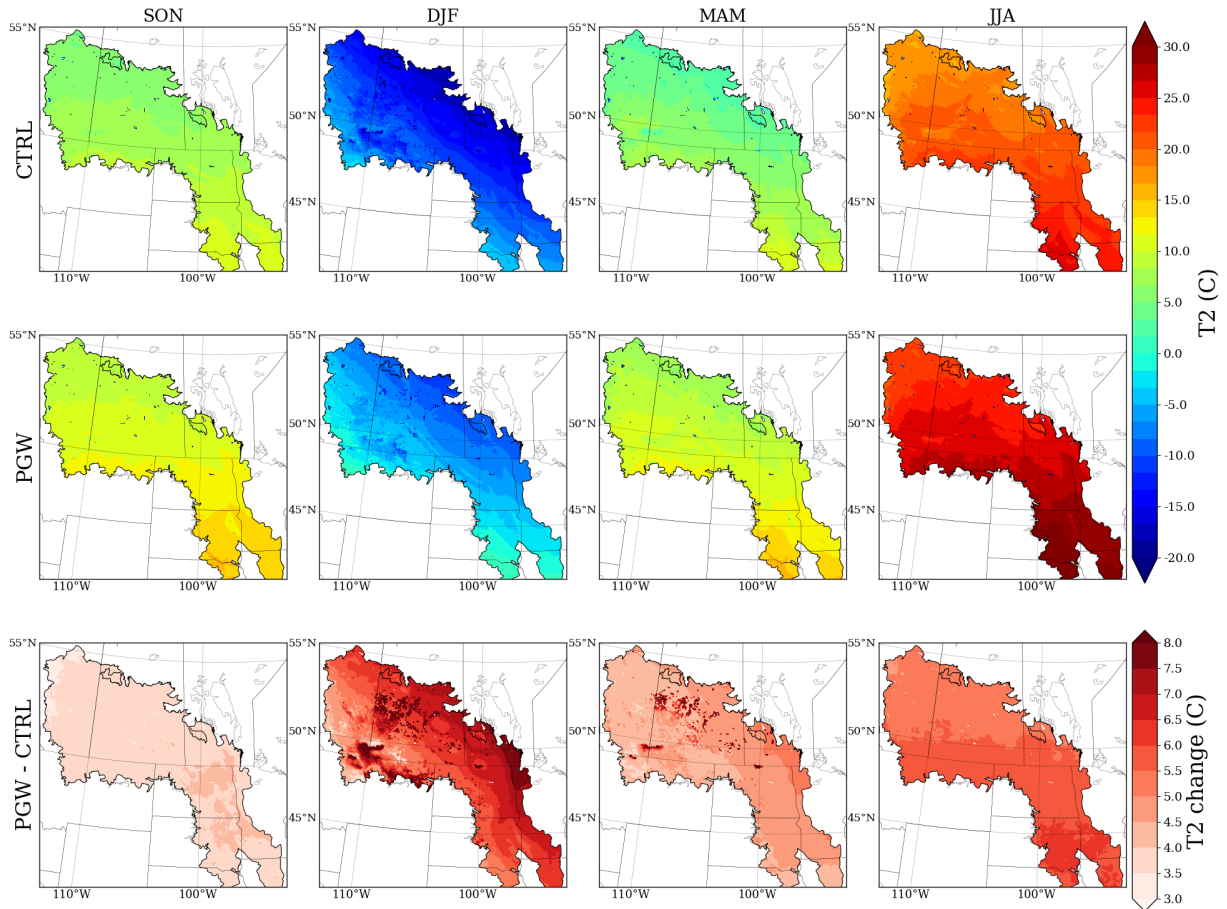
765

Fig. 3 Evaluation of the annual precipitation from two model products (b, f), WRF CONUS and NARR against rain gauge observation (a, e), their bias (c, g) and percentage bias (d, h).



766
 767
 768
 769

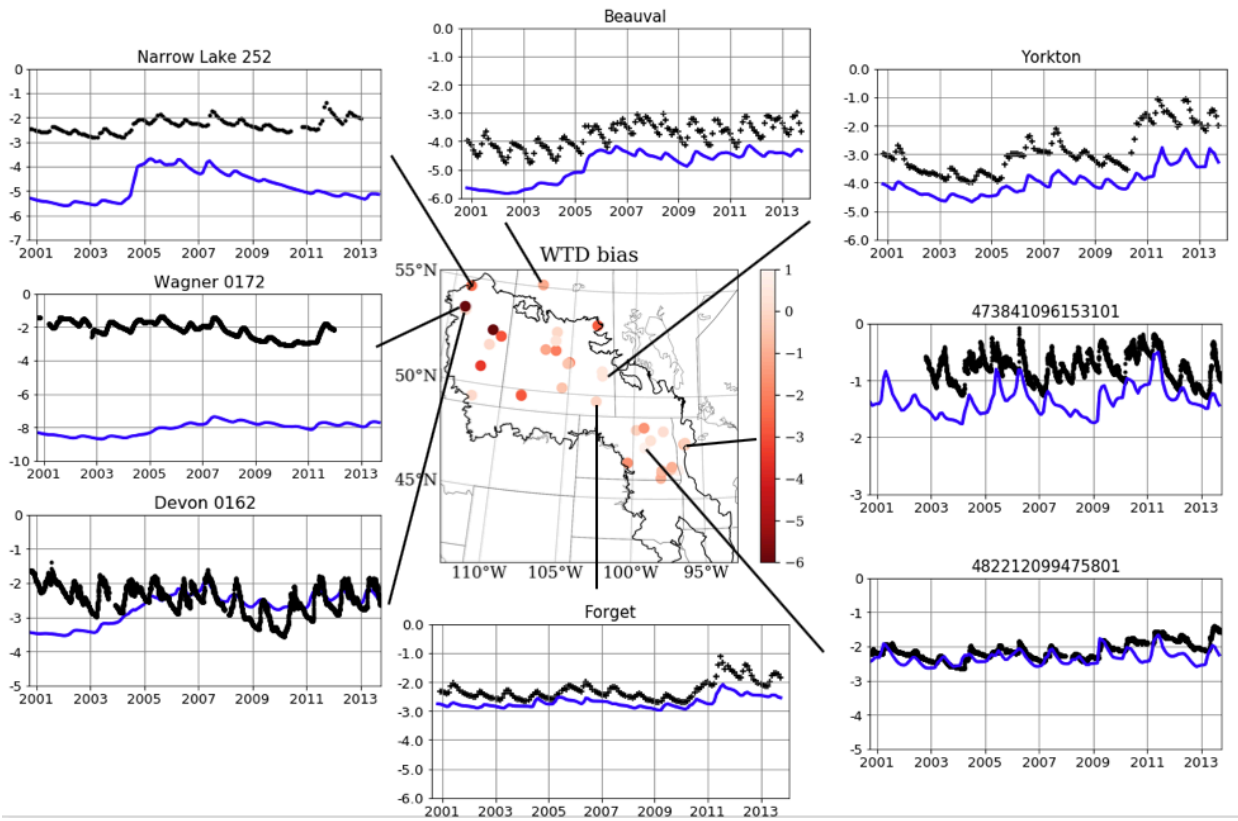
Fig. 4 Seasonal Accumulated precipitation from current climate (CTRL, top), future climate (PGW, middle) and projected change (PGW-CTRL, bottom) in forcing data.



770
 771
 772
 773

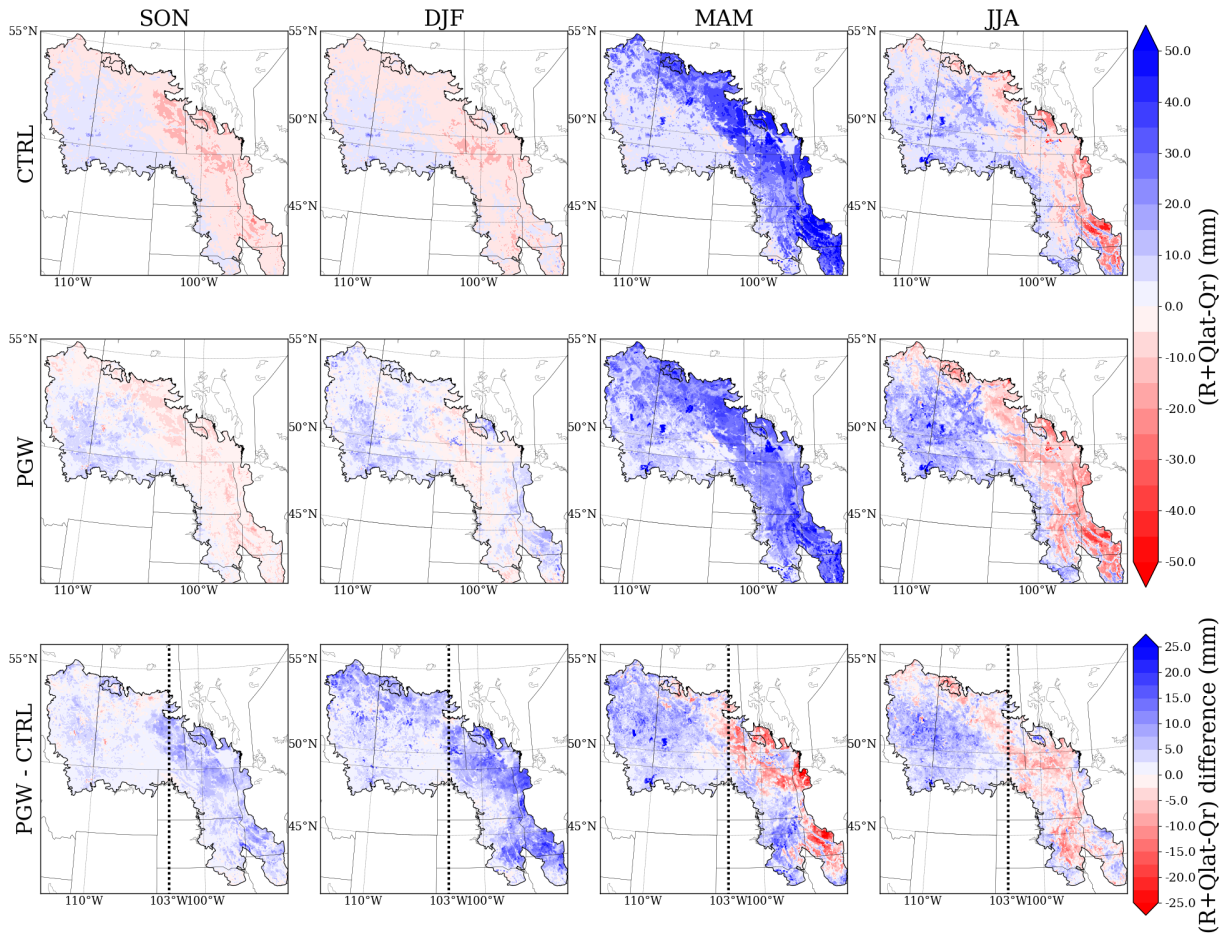
Fig. 5 Seasonal temperatures from current climate (CTRL, top), future climate (PGW, middle) and projected change (PGW-CTRL, bottom) in forcing data.

774



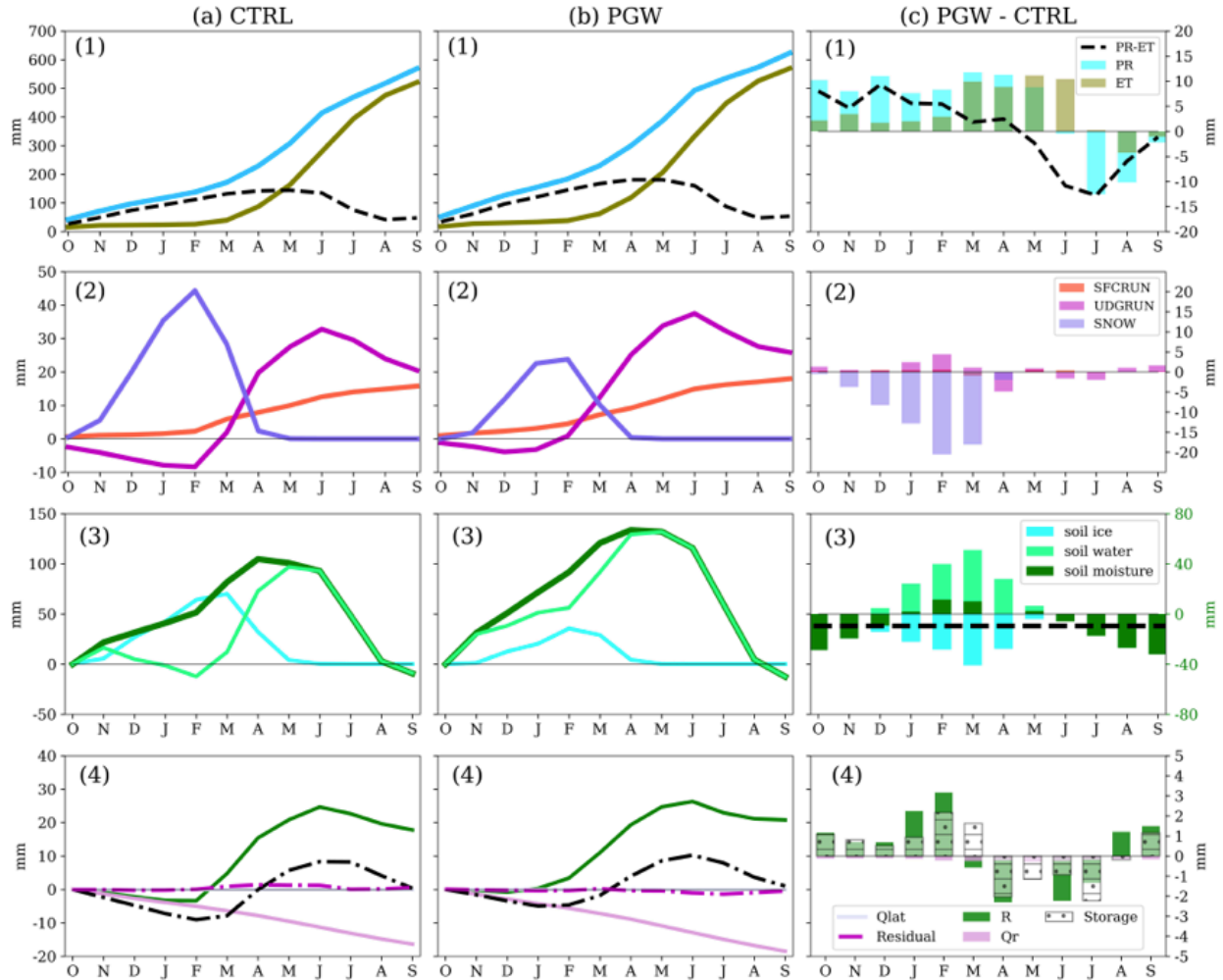
775
776
777
778
779

Fig. 6. WTD (m) bias from CTRL simulation and timeseries from 8 groundwater wells in PPR. See Table 2 CTRL column for the model statistics and supplemental materials for complete timeseries from 33 wells.



780
781
782
783
784

Fig. 7 Seasonal accumulated total groundwater fluxes ($R+Q_{lat} - Q_r$) for current climate (CTRL, top), future climate (PGW, middle) and projected change (PGW-CTRL, bottom) in forcing data. Black dashed lines in PGW-CTRL separate the PPR into eastern and western halves.



storage change: 1.763 mm
 recharge change: 4.152 mm
 river flux change: 2.260 mm
 lateral flux change: -0.001 mm

785

786

787

788

789

790

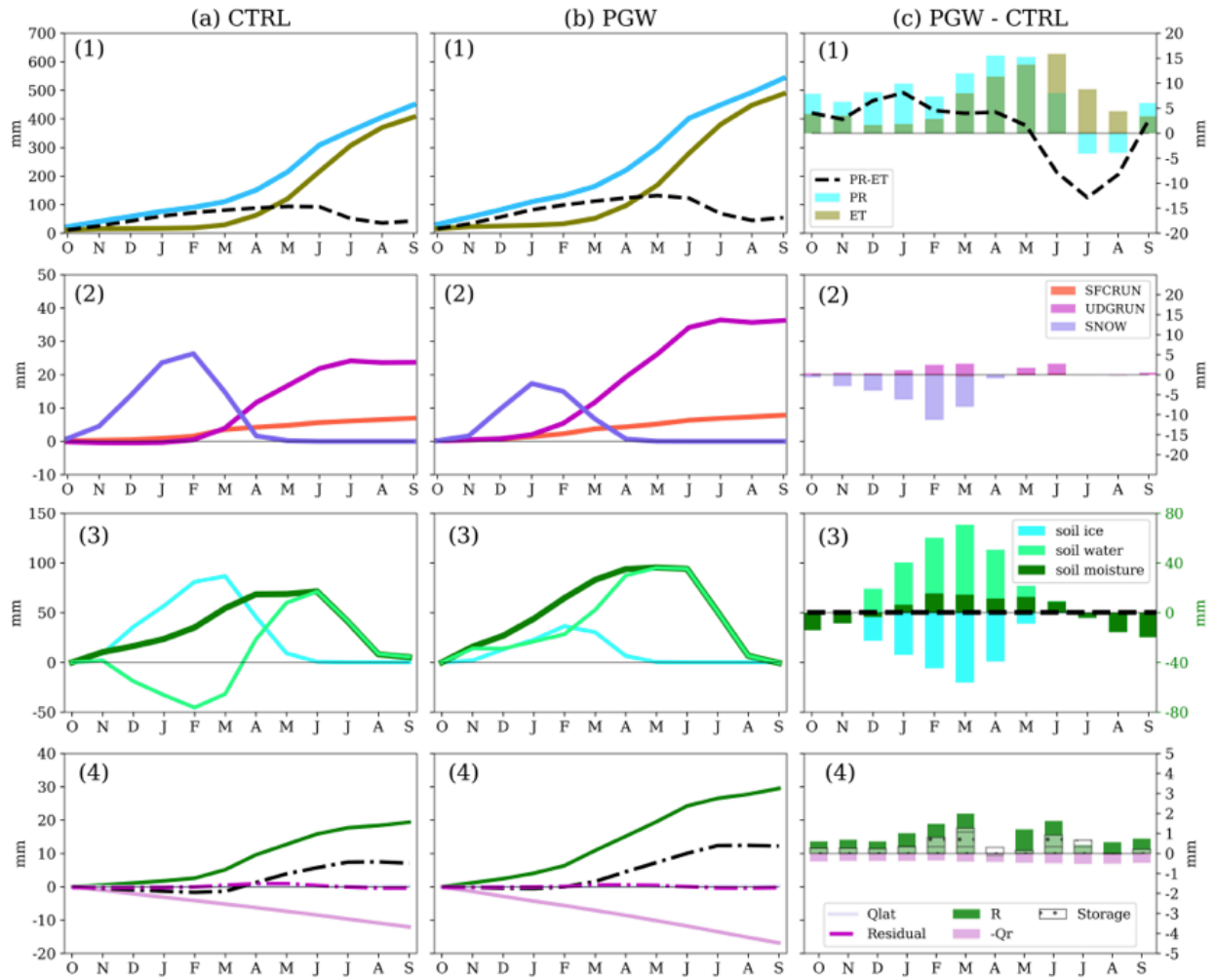
791

792

793

794

Fig. 8 Water budget analysis in the eastern PPR in (a) CTRL, (b) PGW and (c) PGW – CTRL. Water budget terms include: (1) *PR* & *ET*, (2) surface snow, surface runoff and underground runoff (*SNOW*, *SFCRUN*, and *UDGRUN*), (3) change of soil moisture storage (soil water, soil ice and total soil moisture, ΔSMC) and (4) groundwater fluxes and the change of groundwater storage (R , Q_{lat} , Q_r , ΔS_g). The annual mean soil moisture change (PGW-CTRL) is shown with black dashed line in (3). The Residual term is defined as $Res = (R + Q_{lat} - Q_r) - \Delta S_g$ in (4). Note that in (a) and (b) the accumulated fluxes and change in storage are shown in lines, whereas in (c) the difference in (PGW-CTRL) is shown for each individual month in bars.



storage change: 5.390 mm
 recharge change: 10.727 mm
 river flux change: 5.207 mm
 lateral flux change: 0.000 mm

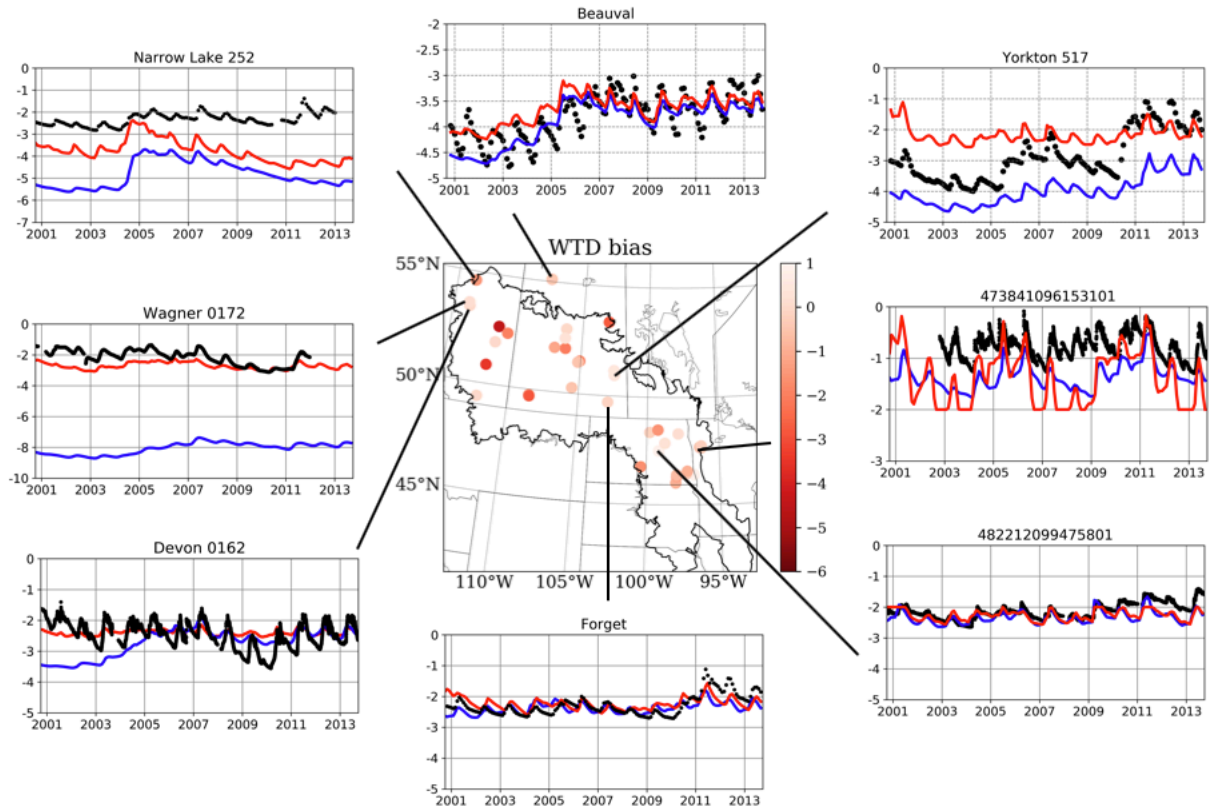
795

796

797

798

Fig. 9 Same as Fig. 8, but for the western PPR.



799
 800 **Fig. 10** Same as Fig. 6, the timeseries of simulated WTD from both default model (blue) and replacing
 801 soil type simulation, REP (red). REP is the additional simulation by replacing the default soil type in the
 802 model with sandy soil type.
 803
 804